**PERIODICO di MINERALOGIA**
*established in 1930*

Dipartimento di Scienze della Terra
Sapienza Università di Roma

*An International Journal of*
Mineralogy, Crystallography, Geochemistry,
Ore Deposits, Petrology, Volcanology
and applied topics on Environment, Archaeometry and Cultural Heritage

# Introducing semi-gem quality blue corundum from the Alvand complex, Hamedan, west Iran

Fariba Sajjadi Alehashem [1,*], Mohssen Moazzen [1,2], Ahmad Jahangiri [1]

[1] Department of Earth Sciences, University of Tabriz, 51666, Tabriz, Iran
[2] School of Arts and Sciences, University of Central Asia, Khorog, 736000, Tajikistan

**ARTICLE INFO**

Submitted: February 2020
Accepted: October 2020
Available on line: January 2021

* Corresponding author:
fariba.sadjadi@yahoo.com

Doi: 10.13133/2239-1002/17315

How to cite this article:
Sajjadi Alehashem F. et al. (2021)
Period. Mineral. 90, 195-209

**ABSTRACT**

Semi-gem quality corundum crystals are formed in a syenite pegmatite dyke in the Alvand igneous-metamorphic complex in west Iran. The dyke is intruded the igneous rocks and the surrounding hornfelses. Corundum is mainly associated with K-feldspar in the rocks and makes crystals 2 to 60 mm across. It shows grey, bluish-grey, pale blue, ink blue and dark blue colours. The crystals show colour zoning and trapiche-like zoning in hand specimens and under the microscope. The main mineral phase inclusions in corundum crystals are muscovite, biotite, hercynite and Nb-Ta oxides. LA-ICP-MS and electron microprobe analyzes indicate wide range of Fe/Mg, Fe/Ti, Ti/Mg and Ga/Mg ratios for the analyzed crystals while variation of Cr/Ga ratio is limited. The geological evidence, mineral inclusions and mineral chemistry characteristics such as high Fe and Ga and low Mg and Cr contents suggest a magmatic origin for these corundum crystals. $Ti^{4+}$-$Fe^{2+}$ exchange was found as the main factor controlling the colour variation in the corundum crystals.

Keywords: Corundum; Blue Sapphire; Pegmatite; Alvand; Hamedan, Iran.

## INTRODUCTION

Corundum with formula of $Al_2O_3$ is a member of the hematite group of oxide minerals along with hematite ($Fe_2O_3$), eskolaite ($Cr_2O_3$), karelianite ($V_2O_3$) and tistarite ($Ti_2O_3$). There is no solid-solution series among these minerals (Cesborn et al., 2002). Corundum is common in silica-deficient igneous and metamorphic rocks. It occurs in alkali basalts (Levinson and Cook, 1995; Sutherland et al., 1998; Sutthirat et al., 2001; Zaw et al., 2006), contact metamorphic rocks (Droop and Moazzen, 2007), high grade regional metamorphic rocks (Kelly and Harley, 2004) and metabauxites (Feenstra, 1996, Aydoğan and Moazzen, 2012). Gem quality large corundum crystals are rare. The main resources are alkaline basalts from SE Asia, NE Australia and Africa (Simonet et al., 2008). Deer et al. (1992) and Klein and Hurlbert (1993) consider syenite magma as the major corundum crystalizing magma. However, gem quality corundum in intermediate igneous rocks are rare and some examples include corundum-bearing monzonite from the Dusi deposit, known as Garba Tula syenite in Kenya (Simonet et al., 2004), Ilmen sapphire-bearing syenite in south Ural Mountains, Russia (Vysotskiy et al., 2015; Sorokino et al., 2017) and Haliburton, Bancroft, Dungannon deposits in Ontario, Canada (Grice, 1989), India (Coimbatore, Madras) and Norway (Seiland, Finmark) (Giuliani et al., 2014).

The igneous and metamorphic complex of Alvand, south of Hamedan city in west Iran has been subjected to many studies (Baharifar et al., 2004; Sepahi et al., 2004; Shahbazi et al., 2010; Saki et al., 2012; Sepahi et al., 2018), however there is no report on occurrence of semi-gem quality corundum in these publications. Sepahi et al. (2020) mentioned the occurrence of corundum in Alvand pegmatites but their study is focused on petrology of granitoids and pegmatites. We report for the first time, semi-gem quality corundum from this complex and from

Iran and the west Asia. The field occurrence, petrography, mineral phase inclusions and mineral chemistry of this corundum occurrence are studied here. The origin of the crystals and factor controlling the colour are addressed.

## ANALYTICAL METHODS

Major element analyzes of corundum-bearing pegmatite (CBP) and Alvand granitoids were carried out on fused lithium tetra borate glass disks using X-ray fluorescence spectrometer PANalytical AxiosmAX fitted with a 4,0 KW Rh X-ray tube. Loss on ignition (LOI) was determined based on mass difference of 2 grams of dried powdered rock before and after heating in 850 ˚C for 4 hours. 4 samples of CBP and 2 samples of Alvand granitoids were analyzed and the results are listed in Table 1.

Field emission (Shottky-FE) SEM equipped with SE, in-lens SE and BSE detectors was used for imaging and analyzes. EDX analyses were performed using a Penta-FET 3x detector, monitored by the AZtec 2.4 software package released by Oxford Instruments. Some of EDX analyses of corundum mineral inclusions are listed in Table 2.

Major element analyzes of corundum were carried out by electron probe micro analysis (EPMA) on thin-polished section. A five wavelength dispersive spectrometers, using a field emission gun equipped with JEOL JXA-8530F Hyper Probe (15 kV, 15 nA, 3µm) was used. Counting time was 30s on peaks and 15s on background. Natural silicates and oxides were used for the calibration. Repeated analyzing of the standards as unknown samples at the beginning of each analytical session and during the session gave precision of <2% for the results. The analytical data were corrected with the phi-rho-Z matrix correction following Armstrong (1995). 60 points through two profiles on corundum crystals were analyzed. The results are listed in Table 3.

Trace element of corundum and REE of corundum and tourmaline determinations were made *in situ*, using laser ablation inductively coupled plasma-mass spectrometry (LA-ICP-MS) on an ELEMENT XR system interfaced to a NewWave UP-193 ArF excimer ablation system. Ablation was performed with ablation ejecta being introduced into the ICP plasma by an Ar gas-stream. Data were acquired using a 100µm diameter spot for corundum and 50µm diameter spot for tourmaline, pulsing the laser at 10Hz producing an energy density on the sample of the order of 6 J/cm$^2$. External standardization was performed by analysis of SRM 612, using an 80 µm diameter spot with linear scan 20 µm/s speeds. Data of corundum and tourmaline were reduced using $Al_2O_3$ 100% and $Al_2O_3$ 30.83% respectively, determined with EMPA, as an internal standard. Analyzes for corundum trace elements were performed on four polished-thick sections (100 µm) and 56 points of the corundum crystals were analyzed for which data are listed in Table 4. 10 points of the tourmaline crystals and 3 points of corundum crystals were analyzed for REE for which data are listed in Table 5.

REE of CBP and Alvand granitoids determinations were made using LA-ICP-MS spectrometry on fused lithium tetra borate glass disks. The quadrupole spectrometer Agilent 7700 is interfaced to a GeoLas 200M ArF excimer ablation system. The on-sample laser beam fluence and irradiance were set at 7 J/cm$^2$ and 1.41 GW/cm$^2$, respectively at a laser pulse repetition rate of 10 Hz. The pit size was 150 µm and helium was used as a carrier gas. Background and signal were measured 90 and 50 seconds, respectively. Three points were measured on each glass and results were averaged. Calcium that previously determined by XRF, was used as internal standard. The SRM 612 soda-lime-silica glass standard was used as external standard. 4 samples of CBP and 2 samples of Alvand granitoids were analyzed and data are listed in Table 5.

All sample preparations and analyses were carried out at the University of Lausanne, Switzerland.

Table 1. XRF analyzes of granitoids and corundum-bearing pegmatite (CBP) for major elements (wt %) from the Alvand complex.

| Sample | Rock/Mineral type | Crn | $SiO_2$ | $TiO_2$ | $Al_2O_3$ | $Fe_2O_3$ | MnO | MgO | CaO | $Na_2O$ | $K_2O$ | $P_2O_5$ | Total | LOI |
|---|---|---|---|---|---|---|---|---|---|---|---|---|---|---|
| SH1 | granitoid | in contact with CBP | 58.78 | 0.47 | 20.27 | 4.78 | 0.11 | 0.20 | 1.71 | 6.77 | 4.62 | 0.04 | 97.75 | 0.38 |
| SH16 | granitoid | not in contact with CBP | 62.34 | 0.62 | 16.9 | 5.55 | 0.11 | 0.24 | 5.08 | 5.00 | 2.24 | 0.06 | 98.14 | 0.57 |
| CP13 | CBP | ~30% v | 56.36 | 0.05 | 29.39 | 0.94 | 0.03 | 0.03 | 0.41 | 5.58 | 6.14 | 0.03 | 98.90 | 1.27 |
| CP26 | CBP | ~30% v | 55.84 | 0.05 | 29.96 | 1.20 | 0.03 | 0.01 | 0.41 | 5.58 | 5.55 | 0.03 | 98.63 | 1.31 |
| CP46 | CBP | ~15% v | 61.52 | 0.05 | 22.00 | 1.67 | 0.06 | 0.01 | 1.55 | 6.2 | 5.77 | 0.01 | 98.84 | 1.01 |
| CP47 | CBP | ~3% v | 66.54 | 0.03 | 18.92 | 0.45 | 0.02 | 0.01 | 1.67 | 6.08 | 5.08 | 0.01 | 98.80 | 0.29 |

Table 2. SEM-EDX analyzes of mineral inclusions of corundum crystals (wt%).

| Mineral | O | Si | Al | Ca | Na | K | Mg | Fe | Mn | Zn | Ag | Ti | P | La | Ce | Nb | Ta | Nd | Th | U | C | Total |
|---|---|---|---|---|---|---|---|---|---|---|---|---|---|---|---|---|---|---|---|---|---|---|
| allanite | 44.3 | 13.7 | 9.6 | 6.6 | - | - | - | 7.8 | 1.3 | - | 0.6 | - | - | 5.0 | 8.8 | - | - | 2.6 | - | - | - | 100.3 |
| allanite | 43.6 | 12.8 | 9.4 | 6.0 | - | - | - | 9.0 | 1.3 | - | 1.2 | - | - | 5.0 | 8.5 | - | - | 3.2 | - | - | - | 100.0 |
| Nb-Ta oxide (colombite) | 31.7 | - | - | - | - | - | - | 12.8 | 3.3 | - | - | 1.0 | - | - | - | 43.8 | 7.4 | - | - | - | - | 100.0 |
| Nb-Ta oxide (colombite) | 32.8 | - | - | - | - | - | - | 12.9 | 3.2 | - | - | 0.9 | - | - | - | 45.7 | 4.5 | - | - | - | - | 100.0 |
| Nb-Ta oxide (colombite) | 34.5 | - | - | - | - | - | - | 14.1 | 2.7 | - | - | 1.3 | - | - | - | 44.0 | 3.5 | - | - | - | - | 100.1 |
| Nb-Ta oxide (colombite) | 32.3 | - | - | - | - | - | - | 15.0 | 2.7 | - | - | - | - | - | - | 48.0 | 1.9 | - | - | - | - | 99.9 |
| Apatite | 43.0 | - | - | 35.2 | - | - | - | - | - | - | - | - | 15.1 | - | - | - | - | - | - | - | 6.8 | 100.1 |
| U-Th aluminous oxide | 28.3 | 1.0 | 14.4 | - | - | - | - | 1.6 | - | - | - | - | - | | - | - | - | - | 23.6 | 30.9 | - | 99.8 |
| (Zn.Fe) spinel | 41.7 | - | 27.6 | - | - | - | - | 17.8 | 0.6 | 12.4 | - | - | - | | - | - | - | - | - | - | - | 100.1 |
| (K.Na) white mica | 52.8 | 18.9 | 19.2 | - | 0.5 | 8.0 | - | 0.6 | - | - | - | - | - | | - | - | - | - | - | - | - | 100.0 |
| (K.Na) white mica | 52.4 | 18.5 | 20.1 | 0.9 | 0.6 | 7.0 | - | 0.6 | - | - | - | - | - | | - | - | - | - | - | - | - | 100.1 |
| Fe-biotite | 45.5 | 12.8 | 11.1 | - | - | 6.8 | 0.4 | 22.8 | - | - | - | 0.6 | - | - | - | - | - | - | - | - | - | 100.0 |

## GEOLOGY AND DESCRIPTION OF THE CORUNDUM-BEARING PEGMATITE (CBP) DYKE

The Alvand complex is located in the Sanandaj-Sirjan plutonic-metamorphic zone of Iran (Mehdipour Ghazi and Moazzen, 2015), which is the imbricate zone of the Zagros Orogen and is formed during Neotethys oceanic crust subduction beneath the Iranian microcontinent (Mohajjel and Fergusson, 2000; Shahabpour, 2005). This zone is comprised of low (greenschist) to high grade (upper amphibolite) regional metamorphic rocks, intruded by mainly intermediate to felsic plutons and resulted contact aureoles. The main rock types of the Alvand complex are granite granodiorite, tonalite and mafic rocks with gabbro and gabbro-norite compositions (Shahbazi et al., 2010). U-Pb dating on zircons from granitoids indicate Jurassic as the age of emplacement, and crystallization of gabbros occurred 166 Ma ago (Shahbazi et al., 2010). The country rocks are known as Hamedan phyllite (Mohajjel et al., 2003). They are metamorphosed thermally within the Alvand aureole to different degrees and diverse contact metamorphic mineral zones are developed in the pelitic protolith (Sepahi et al., 2004; Saki et al., 2012; Sepahi et al., 2018) (Figure 1). A N20E trending pegmatite dyke, about 80 m long and 1-2 m thick is intruded the contact metamorphic rocks (andalusite, garnet and cordierite-bearing hornfels) and the Alvand granitoid, at south of Hamedan (Figure 2a). Corundum-bearing pegmatite (CBP) dyke contains grey to blue corundum, 2-60 mm across. The contact between the dyke and the granitoid is not sharp and has a curvature and zigzag pattern, implying its intrusion, while the granitoid was still warm. Distributions of corundum crystals in the pegmatitic dyke do not show any order or orientation, but they are more clustered at the contact of the dyke with the country rocks (Figure 2b). No corundum was found in the host granitoid and also in the metamorphic rocks of the study area.

According to Sepahi et al. (2020), the composition of Alvand granitoid is mainly quartz-monzonite and composition of granitoid at the contact with CBP is syenite. Our study shows that Alvand granitoid at the contact with CBP is alkaline syenite (Figure 3). Samples from the main granitoid body studied by Sepahi et al. (2020) are granite to quartz-diorite (granodiorite, Figure 3).

The analyzed corundum-bearing pegmatite samples plot in the syenite and nepheline syenite fields of diagram in Figure 3. No feldspathoid was found in the samples. Samples (CP13 and 26) with high corundum content (up to 35 volume%), which are dark grey in colour, plot in the nepheline syenite field, while pale coloured samples with less corundum content (15 volume%, sample CP46 and 3 volume%, sample CP47) plot in the syenite field (Figure 3).

The syenite pegmatite samples from the dyke are

Table 3. EPMA analyzes of the corundum for major elements (wt %). Analyzes are carried out on two traverses (lines 2 and 3) along two corundum crystals in Sample CP21.

| Sample | $Al_2O_3$ | $Na_2O$ | $SiO_2$ | MnO | $Cr_2O_3$ | $TiO_2$ | FeO | CaO | Total |
|---|---|---|---|---|---|---|---|---|---|
| 2 Line 01 | 100.74 | 0.00 | 0.01 | 0.00 | 0.02 | 0.04 | 0.17 | 0.00 | 100.98 |
| 2 Line 02 | 100.46 | 0.00 | 0.01 | 0.00 | 0.01 | 0.05 | 0.17 | 0.00 | 100.68 |
| 2 Line 03 | 100.58 | 0.00 | 0.01 | 0.00 | 0.01 | 0.06 | 0.20 | 0.00 | 100.86 |
| 2 Line 04 | 100.51 | 0.00 | 0.01 | 0.00 | 0.03 | 0.06 | 0.18 | 0.00 | 100.79 |
| 2 Line 05 | 100.71 | 0.00 | 0.01 | 0.00 | 0.00 | 0.05 | 0.16 | 0.00 | 100.93 |
| 2 Line 06 | 100.66 | 0.00 | 0.00 | 0.00 | 0.00 | 0.32 | 0.17 | 0.00 | 101.15 |
| 2 Line 07 | 100.59 | 0.00 | 0.01 | 0.02 | 0.00 | 0.30 | 0.17 | 0.00 | 101.09 |
| 2 Line 08 | 100.50 | 0.01 | 0.01 | 0.01 | 0.01 | 0.30 | 0.19 | 0.00 | 101.03 |
| 2 Line 09 | 100.54 | 0.03 | 0.01 | 0.00 | 0.00 | 0.36 | 0.18 | 0.00 | 101.12 |
| 2 Line 10 | 100.63 | 0.02 | 0.00 | 0.02 | 0.00 | 0.31 | 0.17 | 0.00 | 101.14 |
| 3 Line 01 | 100.79 | 0.00 | 0.01 | 0.01 | 0.00 | 0.03 | 0.15 | 0.00 | 100.98 |
| 3 Line 02 | 99.95 | 0.01 | 0.01 | 0.00 | 0.00 | 0.07 | 0.18 | 0.00 | 100.21 |
| 3 Line 03 | 100.61 | 0.00 | 0.01 | 0.00 | 0.00 | 0.07 | 0.15 | 0.00 | 100.86 |
| 3 Line 04 | 101.17 | 0.00 | 0.01 | 0.00 | 0.01 | 0.08 | 0.16 | 0.00 | 101.43 |
| 3 Line 05 | 100.47 | 0.00 | 0.01 | 0.00 | 0.00 | 0.18 | 0.16 | 0.00 | 100.83 |
| 3 Line 06 | 100.55 | 0.00 | 0.01 | 0.00 | 0.00 | 0.19 | 0.16 | 0.00 | 100.91 |
| 3 Line 07 | 100.25 | 0.00 | 0.01 | 0.00 | 0.00 | 0.19 | 0.16 | 0.00 | 100.61 |
| 3 Line 08 | 101.01 | 0.00 | 0.01 | 0.00 | 0.01 | 0.17 | 0.17 | 0.00 | 101.37 |
| 3 Line 09 | 100.95 | 0.01 | 0.00 | 0.00 | 0.02 | 0.18 | 0.17 | 0.00 | 101.33 |
| 3 Line 10 | 100.55 | 0.00 | 0.01 | 0.00 | 0.00 | 0.20 | 0.15 | 0.00 | 100.90 |
| 3 Line 11 | 100.61 | 0.00 | 0.01 | 0.01 | 0.00 | 0.19 | 0.17 | 0.01 | 101.00 |
| 3 Line 12 | 100.47 | 0.00 | 0.01 | 0.00 | 0.00 | 0.19 | 0.18 | 0.01 | 100.87 |
| 3 Line 13 | 100.58 | 0.01 | 0.00 | 0.00 | 0.00 | 0.18 | 0.17 | 0.00 | 100.94 |
| 3 Line 14 | 100.66 | 0.00 | 0.00 | 0.00 | 0.00 | 0.19 | 0.16 | 0.00 | 101.02 |
| 3 Line 15 | 100.43 | 0.00 | 0.01 | 0.01 | 0.01 | 0.19 | 0.16 | 0.00 | 100.80 |
| 3 Line 16 | 100.48 | 0.00 | 0.00 | 0.00 | 0.01 | 0.20 | 0.18 | 0.00 | 100.87 |
| 3 Line 17 | 100.46 | 0.00 | 0.01 | 0.00 | 0.00 | 0.20 | 0.16 | 0.00 | 100.83 |
| 3 Line 18 | 100.52 | 0.02 | 0.01 | 0.00 | 0.00 | 0.19 | 0.17 | 0.00 | 100.90 |
| 3 Line 19 | 99.76 | 0.01 | 0.01 | 0.01 | 0.00 | 0.20 | 0.16 | 0.00 | 100.14 |
| 3 Line 20 | 100.52 | 0.00 | 0.01 | 0.00 | 0.01 | 0.19 | 0.17 | 0.00 | 100.90 |
| 3 Line 21 | 100.44 | 0.00 | 0.00 | 0.00 | 0.01 | 0.19 | 0.15 | 0.00 | 100.78 |
| 3 Line 22 | 100.56 | 0.00 | 0.00 | 0.00 | 0.01 | 0.19 | 0.17 | 0.00 | 100.93 |
| 3 Line 23 | 100.10 | 0.00 | 0.01 | 0.00 | 0.00 | 0.19 | 0.17 | 0.00 | 100.46 |
| 3 Line 24 | 100.62 | 0.00 | 0.01 | 0.01 | 0.02 | 0.20 | 0.17 | 0.00 | 101.04 |
| 3 Line 25 | 100.27 | 0.00 | 0.02 | 0.01 | 0.00 | 0.18 | 0.18 | 0.00 | 100.66 |
| 3 Line 26 | 100.91 | 0.01 | 0.01 | 0.00 | 0.01 | 0.01 | 0.13 | 0.00 | 101.07 |
| 3 Line 28 | 98.77 | 0.00 | 0.01 | 0.00 | 0.01 | 0.02 | 0.12 | 0.00 | 98.93 |
| 3 Line 31 | 100.65 | 0.00 | 0.01 | 0.00 | 0.00 | 0.03 | 0.13 | 0.00 | 100.81 |
| 3 Line 32 | 101.14 | 0.00 | 0.01 | 0.00 | 0.01 | 0.03 | 0.14 | 0.00 | 101.33 |
| 3Line 33 | 101.15 | 0.01 | 0.01 | 0.00 | 0.00 | 0.03 | 0.11 | 0.00 | 101.30 |
| 3 Line 34 | 100.75 | 0.00 | 0.00 | 0.00 | 0.01 | 0.02 | 0.10 | 0.00 | 100.88 |
| 3 Line 35 | 100.69 | 0.00 | 0.01 | 0.01 | 0.00 | 0.01 | 0.13 | 0.01 | 100.86 |
| 3 Line 36 | 100.39 | 0.00 | 0.00 | 0.00 | 0.00 | 0.03 | 0.12 | 0.00 | 100.54 |
| 3 Line 37 | 100.67 | 0.00 | 0.01 | 0.00 | 0.00 | 0.16 | 0.14 | 0.00 | 100.98 |
| 3 Line 38 | 100.64 | 0.00 | 0.01 | 0.00 | 0.01 | 0.15 | 0.16 | 0.00 | 100.97 |
| 3 Line 39 | 100.83 | 0.00 | 0.01 | 0.00 | 0.00 | 0.16 | 0.14 | 0.01 | 101.14 |

Table 3. ... Continued

| Sample | $Al_2O_3$ | $Na_2O$ | $SiO_2$ | MnO | $Cr_2O_3$ | $TiO_2$ | FeO | CaO | Total |
|---|---|---|---|---|---|---|---|---|---|
| 3 Line 40 | 100.27 | 0.01 | 0.01 | 0.01 | 0.02 | 0.16 | 0.13 | 0.01 | 100.59 |
| 3 Line 41 | 100.46 | 0.00 | 0.01 | 0.02 | 0.00 | 0.14 | 0.14 | 0.00 | 100.78 |
| 3 Line 42 | 100.50 | 0.01 | 0.01 | 0.01 | 0.00 | 0.17 | 0.17 | 0.00 | 100.87 |
| 3 Line 43 | 100.44 | 0.00 | 0.01 | 0.01 | 0.02 | 0.14 | 0.16 | 0.00 | 100.78 |
| 3 Line 44 | 100.29 | 0.01 | 0.00 | 0.00 | 0.00 | 0.14 | 0.15 | 0.00 | 100.59 |
| 3 Line 45 | 100.40 | 0.00 | 0.01 | 0.00 | 0.00 | 0.16 | 0.17 | 0.01 | 100.74 |
| 3 Line 46 | 100.39 | 0.00 | 0.00 | 0.00 | 0.00 | 0.14 | 0.11 | 0.00 | 100.65 |
| 3 Line 47 | 100.17 | 0.00 | 0.00 | 0.00 | 0.02 | 0.15 | 0.18 | 0.00 | 100.53 |
| 3 Line 49 | 100.50 | 0.00 | 0.02 | 0.01 | 0.01 | 0.16 | 0.18 | 0.00 | 100.86 |
| 3 Line 50 | 100.70 | 0.00 | 0.01 | 0.01 | 0.00 | 0.13 | 0.14 | 0.00 | 100.99 |

composed mainly of pink K-feldspar and corundum crystals (Figure 4a). Corundum makes ~35 v% of the rock in some parts of the dyke. Quartz and tourmaline are the other abundant minerals in some parts of the dyke samples and show symplectite textures occasionally (Figure 4 b,c). Corundum is not in direct contact with quartz. A reaction rim is developed around corundum, composed of muscovite and biotite (Figure 4d). The presence of this muscovite+biotite or muscovite corona around some corundum crystals indicate the late alteration effects on corundum crystals. Garnet is rare mineral phase in some of the samples.

## CORUNDUM CRYSTALS DESCRIPTION

Most of the studied corundum crystals are opaque to translucent (Figure 5a).The crystals are usually idiomorphic and barrel shaped. 120-degree growth lines can be seen clearly in some crystals (Figure 5 b,c). Other features are polysynthetic twinning and overgrowth. The colour varies from grey, bluish-grey to pale blue and vivid high saturated ink blue. Most of corundum crystals have strong blue to colourless colour zoning (Figure 5 b,c). The ink or vivid high saturated blue colour is present in the core of the corundum crystal in some samples, while the rim is light blue or very light blue (Figure 5b). This relation is apparently changed in some cases due to overgrowth and distortion of the crystals. Dark and ink blue parts do not show a distribution pattern in some samples and they appear as patches in the crystal (Figure 5e). Opaque blue colour is characteristic of corundum in syenites (Giuliani et al., 2014). Some crystals show six-rayed pattern (Figure 5 e,d). These rays usually are inclusion-rich parts, known as trapiche or trapiche-like crystals. According to studies by Giuliani and Pignatelli (2016), the rays are correlated with overgrowth zoning in the trapiche crystals, dividing the crystals to crystallographic sectors. These rays do not correlate with overgrowth zoning in trapiche-like crystals and cut it perpendicularly. The six-rayed pattern for the Hamedan samples is perpendicular to the overgrowth zoning and they are trapiche-like (Figure 5e). The corundum samples are polishable and give nice ornaments. Figure 5d shows a pendent with cabochon polish made from translucent Hamedan sapphire (a type of gem-quality corundum) from Alvand with trapiche-like feature and dark blue colour.

## PETROGRAPHY AND MINERAL PHASE INCLUSIONS

The corundum-bearing pegmatite syenite contains large K-feldspars of microcline with pericline texture (Figure 6a), corundum and sub-ordinate amounts of plagioclase. Corundum in mainly surrounded by K-feldspar and shows reaction textures consisted of muscovite and biotite at the rims (Figure 6 a,b). Muscovite shows two generations of fine-grained crystals (sericite) at the contact with corundum and relatively large flakes away from corundum, at the outer rim (Figure 6b). The reaction rim is made only from muscovite without biotite in some cases. Other mineral phases under the microscope are garnet, hercynite spinel (Figure 6c), tourmaline, zircon (Figure 6d) and oxide minerals. K-feldspar, plagioclase and corundum show granular textures and quartz shows interstitial texture, indicative of crystallization from a liquid phase (magma).

Different types of solid mineral phase inclusions were observed in the corundum crystals. The most frequent mineral inclusions are mica crystals (muscovite, biotite). Tiny hercynite inclusions can be distinguished in hand specimens, while other inclusions were determined under the microscope or by SEM and EDXRF studies. The inclusions under the microscope are biotite, muscovite, hercynite and zircon (Figure 6b, c, d). Muscovite and biotite can be seen around the corundum crystals and along cracks within corundum (Figure 7 a,b).

Opaque mineral inclusions can be seen under the microscope. EDXRF and SEM studies revealed presence of Nb-Ta oxides as inclusions (Figure 7d). Other inclusions

Table 4. LA-ICP-MS analyzes on corundum (ppm). BD: below the detection limit. MgO detection limit: 2.5 ppm, MnO detection limit: 0.3 ppm.

| Sample | Point | MgO | MnO | V | Ga | Nb | Ta |
|---|---|---|---|---|---|---|---|
| CP13 | 6a03 | BD | 75.7 | 1.0 | 415.8 | 8.6 | 2.7 |
| CP13 | 6a04 | 10.0 | 1.6 | 1.1 | 435.6 | 0.7 | 0.5 |
| CP13 | 6a05 | BD | 1.0 | 0.9 | 429.8 | 1.9 | 2.2 |
| CP13 | 6a06 | BD | 1.0 | 1.1 | 474.6 | 2.0 | 1.0 |
| CP13 | 6a07 | BD | 31.9 | 0.9 | 444.6 | 19.4 | 2.2 |
| CP13 | 6a08 | BD | 63.2 | 1.1 | 450.6 | 3.9 | 0.7 |
| CP13 | 6a09 | BD | 1.9 | 1.2 | 454.8 | 1.3 | 0.4 |
| CP13 | 6a10 | BD | 12.9 | 1.1 | 446.2 | 14.1 | 3.3 |
| CP13 | 6a11 | BD | 1.3 | 1.1 | 438.6 | 2.9 | 0.8 |
| CP13 | 6a12 | BD | 1.3 | 1.0 | 439.1 | 2.2 | 0.9 |
| CP13 | 6a13 | BD | 1.2 | 1.0 | 444.2 | 1.8 | 0.6 |
| CP13 | 6a14 | BD | 1.3 | 1.2 | 470.7 | 2.7 | 0.8 |
| CP13 | 6a16 | BD | 13.5 | 1.2 | 473.3 | 27.1 | 2.7 |
| CP13 | 6a17 | BD | 1.4 | 1.0 | 434.2 | 25.8 | 5.9 |
| CP13 | 6a18 | BD | 1.0 | 1.0 | 440.7 | 51.6 | 16.4 |
| CP13 | 6b03 | BD | 1.0 | 1.0 | 465.9 | 11.4 | 2.9 |
| CP13 | 6b05 | 8.7 | 53.7 | 1.0 | 452.4 | 41.7 | 11.1 |
| CP13 | 6b06 | BD | 30.4 | 1.2 | 478.8 | 54.5 | 9.7 |
| CP13 | 6b07 | 2.8 | 0.8 | 1.4 | 447.7 | 0.6 | 0.6 |
| CP10 | 6b08 | 4.1 | 2.3 | 1.0 | 479.2 | 13.0 | 1.4 |
| CP10 | 6b09 | 2.4 | 3.3 | 1.3 | 538.0 | 13.7 | 1.7 |
| CP10 | 6b10 | 4.2 | 8.7 | 1.3 | 599.1 | 9.4 | 1.1 |
| CP10 | 6b11 | 4.7 | 1.1 | 1.1 | 464.5 | 29.0 | 4.2 |
| CP10 | 6b12 | 4.3 | BD | 1.0 | 454.1 | 19.0 | 3.9 |
| CP10 | 6b13 | BD | 14.0 | 0.7 | 419.3 | 19.0 | 1.9 |
| CP10 | 6b14 | BD | 2.1 | 0.7 | 416.5 | 4.5 | 0.4 |
| CP10 | 6b15 | BD | 1.7 | 0.8 | 423.0 | 10.8 | 1.2 |
| CP10 | 6b16 | BD | BD | 0.8 | 416.2 | 3.7 | 0.8 |
| CP10 | 6b17 | 3.0 | 1.6 | 0.7 | 422.5 | 1.1 | 0.4 |
| CP21 | 6c08 | 4.4 | 1.3 | 1.0 | 380.4 | 192.5 | 250.3 |
| CP21 | 6c09 | 5.1 | 1.1 | 1.0 | 371.6 | 5.5 | 11.0 |
| CP21 | 6c10 | 6.3 | 0.8 | 1.0 | 373.0 | 12.3 | 30.4 |
| CP21 | 6c11 | 12.0 | 0.9 | 1.0 | 370.7 | 26.3 | 50.9 |
| CP21 | 6c12 | BD | 1.4 | 1.0 | 392.1 | 29.7 | 43.9 |
| CP21 | 6c13 | BD | 0.9 | 1.0 | 369.4 | 21.0 | 33.3 |
| CP21 | 6c14 | BD | 1.0 | 1.3 | 371.5 | 386.1 | 664.6 |
| CP21 | 6c15 | BD | BD | 1.4 | 355.5 | 44.3 | 311.4 |
| CP21 | 6c16 | 5.2 | 1.1 | 0.9 | 336.1 | 9.3 | 24.8 |
| CP21 | 6c17 | 4.3 | 2.5 | 0.9 | 333.4 | 4.0 | 13.0 |
| CP21 | 6c18 | 6.4 | 2.2 | 1.4 | 464.1 | 9.7 | 21.6 |
| CP21 | 6d03 | 6.0 | 1.1 | 1.0 | 346.1 | 3.5 | 8.9 |
| CP21 | 6d04 | BD | 2.6 | 0.8 | 299.1 | 23.2 | 61.9 |
| CP21 | 6d05 | BD | 0.7 | 1.1 | 325.5 | 780.2 | 1138.8 |
| CP21 | 6d06 | 4.0 | BD | 0.8 | 291.1 | 3.8 | 11.7 |
| CP21 | 6d07 | 4.7 | 1.6 | 0.9 | 321.2 | 18.9 | 36.2 |
| CP21 | 6d08 | BD | 0.7 | 0.8 | 316.5 | 17.4 | 27.5 |
| CP21 | 6d09 | BD | 1.7 | 0.9 | 319.6 | 2.2 | 6.4 |
| CP21 | 6d10 | 4.8 | BD | 0.7 | 298.7 | 1.6 | 3.4 |
| CP23 | 6d11 | 5.9 | 1.0 | 0.8 | 334.5 | 5.4 | 0.7 |
| CP23 | 6d12 | 3.9 | 0.9 | 0.7 | 302.9 | 5.1 | 1.6 |
| CP23 | 6d13 | 3.9 | 1.6 | 0.5 | 303.9 | 2.5 | 0.5 |
| CP23 | 6d14 | 6.2 | 0.9 | 0.5 | 299.3 | 6.5 | 1.6 |
| CP23 | 6d15 | 7.3 | 1.3 | 0.8 | 279.9 | 67.0 | 11.4 |
| CP23 | 6d16 | 3.8 | 167.1 | 0.8 | 281.5 | 12.1 | 1.6 |
| CP21 | 6d17 | BD | 0.9 | 0.7 | 275.8 | 13.3 | 20.6 |
| CP21 | 6d18 | BD | 0.8 | 0.7 | 217.1 | 1.8 | 6.6 |

found by SEM studies are spinel (Figure 7c), allanite and apatite (Figure 7d) and U-Th aluminous oxides.

## CORUNDUM MINERAL CHEMISTRY

The studied corundum crystals are Ga-rich and V- and Cr-poor. The electron probe micro analyzes are provided in Table 3. Fe content of the analyzed samples vary from 716 to 1379 ppm, Si content is 0-83 ppm, Ti content is 38-2168 ppm and Cr content is 0 to 192 ppm. LA-ICP-MS analyzes results (Table 4) indicate Ga content for the studied corundums of 217 to 599 ppm with an average of 394 ppm and Nb content 0.6 to 767 ppm. The Ta content is 0.36-61.91 ppm and the V content varies from 0.51 to 1.42 ppm.

Ti content in the studied corundum crystals can be divided into three groups. (i) low Ti contents (37.77-474.21 ppm), (ii) moderate Ti contents (802.74-1208.01) and high Ti contents (1802.73-2168.43 ppm).

## DISCUSSION AND CONCLUSIONS

Textural relations show that corundum is crystallized from a silica deficient alkaline syenite magma. Corundum crystals from the Alvand complex are barrel-shaped, which is indicative of their magmatic origin (Guo, 1996). Polysynthetic twinning also can show an igneous origin for the studied samples (e.g. Schmetzer, 1987). Muscovite and biotite fringe around some corundum crystals indicate post-magmatic reactions. Presence of Nb-Ta oxides, spinel, zircon, U-Th aluminous oxide as mineral inclusions in Hamedan corundum crystals show good correspondence with magmatic origin (Guo, 1996; Graham et al., 2008).

CBP samples contain quartz-tourmaline symplectites. Some examples of quartz and corundum and/or hercynite associations are high pressure and high temperature granulites (Motoyoshi et al., 1990; Guiraud et al., 1996), pelitic hornfelses (Droop and Moazzen, 2007) and hydrothermally altered quartz porphyritic rocks (Bottrill, 1998). Quartz and corundum are not is direct contact in most of these examples.

Similarly, corundum and quartz in CBP samples of the Alvand are not in mutual contact and occur is separated small microdomains under the microscope. This may point to silica-rich and silica-poor microdomains during the parental magma crystallization. The other possibility that can be speculated is later origin for quartz-tourmaline symplectites, not in equilibrium with corundum-bearing mineral assemblage. This late process as a fluid-assisted process could have caused alteration of corundums at the margins and creation of reaction textures around the crystals.

Rare earth elements (REE) patterns, normalized to chondrite (Nakamura, 1974) for pegmatite, syenite, tourmaline and corundum are compared (Figure 8). There

Table 5. LA-ICP-MS analyzes of granitoid, corundum-bearing pegmatite (CBP), corundum (Crn) and tourmaline in CBP for REE (ppm) from the Alvand complex. BD: below the detection limit. Ho and Tm detection limit: 0.001ppm.

| Rock type | Sample | Points | La | Ce | Pr | Nd | Sm | Eu | Gd | Tb | Dy | Ho | Er | Tm | Yb | Lu |
|---|---|---|---|---|---|---|---|---|---|---|---|---|---|---|---|---|
| Granitoid | SH1 | | 52.05 | 90.60 | 8.62 | 29.71 | 4.72 | 0.79 | 4.04 | 0.58 | 3.66 | 0.72 | 2.01 | 0.29 | 1.88 | 0.25 |
| CBP | CP13 | | 6.20 | 12.90 | 1.10 | 3.19 | 0.51 | 0.12 | 0.39 | 0.07 | 0.36 | 0.08 | 0.22 | 0.07 | 0.37 | 0.06 |
| | CP26 | | 6.87 | 13.72 | 1.15 | 3.39 | 0.38 | 0.06 | 0.44 | 0.06 | 0.38 | 0.07 | 0.28 | 0.06 | 0.42 | 0.05 |
| Crn | CP21 | 6c14 | 0.12 | 0.27 | 0.03 | 0.15 | 0.01 | 0.00 | 0.03 | 0.00 | 0.01 | 0.00 | 0.00 | 0.00 | 0.01 | 0.00 |
| | CP21 | 6d05 | 0.23 | 0.54 | 0.07 | 0.24 | 0.03 | 0.01 | 0.02 | 0.00 | 0.01 | 0.00 | 0.00 | BD | 0.01 | 0.00 |
| | CP23 | 6d16 | 0.05 | 0.12 | 0.02 | 0.05 | 0.02 | 0.00 | 0.04 | 0.00 | 0.04 | 0.01 | 0.03 | 0.00 | 0.04 | 0.00 |
| Tur in CBP | CP23 | 2a09 | 19.51 | 31.22 | 2.57 | 6.38 | 0.70 | 0.09 | 0.18 | 0.02 | 0.05 | 0.01 | 0.01 | 0.01 | 0.16 | 0.04 |
| | CP23 | 2a10 | 8.02 | 14.03 | 1.20 | 3.09 | 0.29 | 0.05 | 0.10 | 0.01 | 0.03 | 0.00 | 0.01 | 0.00 | 0.07 | 0.03 |
| | CP23 | 2a11 | 14.01 | 23.09 | 1.87 | 4.70 | 0.48 | 0.12 | 0.15 | 0.02 | 0.09 | 0.01 | 0.03 | 0.01 | 0.14 | 0.04 |
| | CP23 | 2a12 | 11.21 | 20.74 | 1.46 | 3.51 | 0.31 | 0.06 | 0.07 | 0.01 | 0.09 | 0.01 | 0.03 | 0.01 | 0.12 | 0.05 |
| | CP23 | 2a13 | 6.18 | 10.79 | 0.89 | 2.08 | 0.18 | 0.05 | 0.07 | 0.01 | 0.03 | 0.00 | 0.01 | 0.00 | 0.04 | 0.02 |
| | CP23 | 2a14 | 6.17 | 10.90 | 0.89 | 2.14 | 0.22 | 0.05 | 0.03 | 0.01 | 0.02 | BD | 0.01 | 0.00 | 0.09 | 0.02 |
| | CP23 | 2a15 | 6.26 | 10.60 | 0.87 | 2.26 | 0.26 | 0.06 | 0.07 | 0.01 | 0.04 | 0.01 | 0.03 | 0.01 | 0.07 | 0.02 |
| | CP23 | 2a16 | 8.46 | 14.88 | 1.24 | 3.24 | 0.34 | 0.06 | 0.13 | 0.01 | 0.04 | 0.00 | 0.01 | 0.01 | 0.07 | 0.04 |
| | CP23 | 2a17 | 12.54 | 21.11 | 1.71 | 4.51 | 0.47 | 0.09 | 0.17 | 0.01 | 0.05 | 0.01 | 0.03 | 0.01 | 0.13 | 0.05 |
| | CP23 | 2a18 | 8.13 | 14.07 | 1.19 | 3.22 | 0.28 | 0.04 | 0.09 | 0.01 | 0.05 | 0.00 | 0.01 | 0.01 | 0.11 | 0.03 |

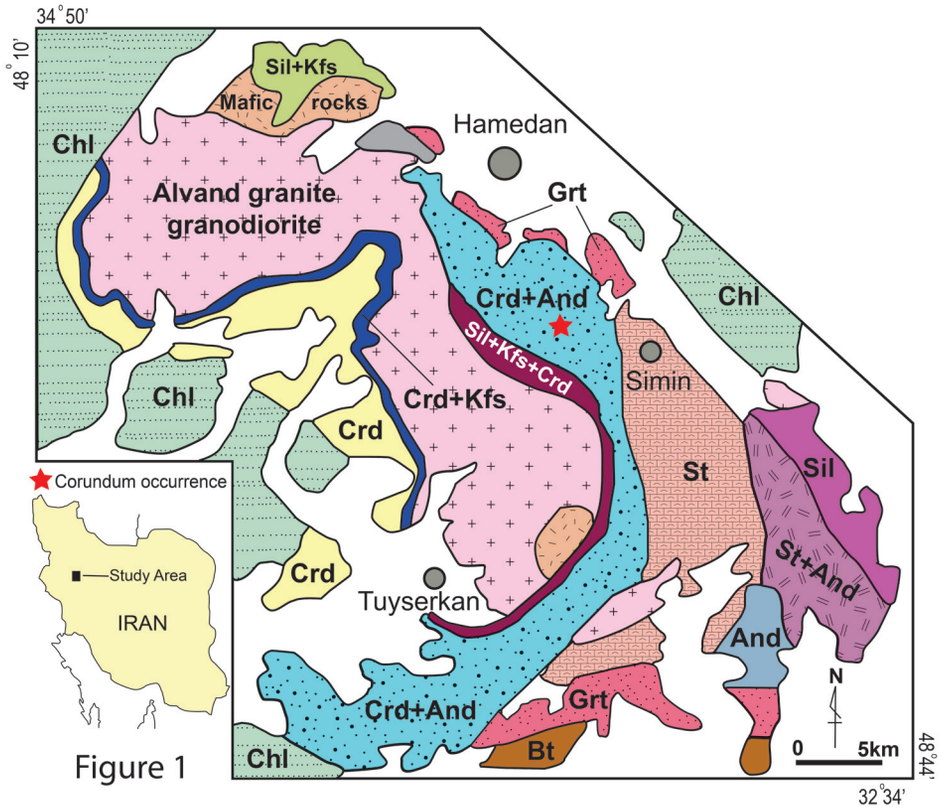


Figure 1

Figure 1. Simplified geological map of the Alvand complex showing the distribution of the metamorphic and igneous rocks (from Sepahi et al., 2018 with modifications). The location of corundum occurrence is shown.

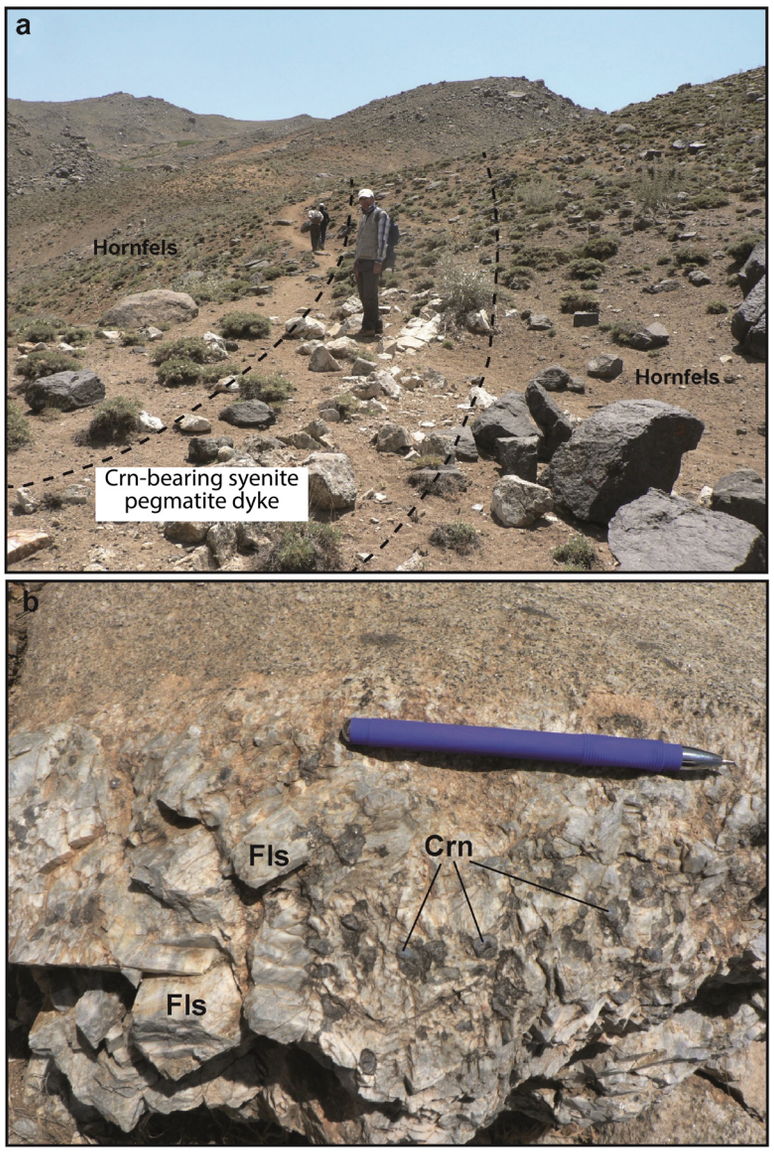


Figure 2. Outcrop of the corundum bearing pegmatite (CBP) dyke (a) and concentration of the corundum crystals at the dyke and country rock contact (b).

is no REE enrichment for corundum crystals, compared to chondrite. The highest REE enrichment relative to chondrite can be seen for sample SH1, which is a syenite sample from the main granitoid body at the contact with the pegmatite dyke. Negative Eu anomaly is evident for the studied samples, except for tourmaline. Corundum shows positive Ho and Gd anomalies, while tourmaline shows negative anomalies for these elements. LREE pattern for tourmaline is similar for those from CBP, while HREE patterns are quite different. LREE/HREE enrichment in tourmaline is evident, while it is not clear for other analyzed samples (they show almost linear trend, Figure 8).

Normalized La/Yb ratio for the analyzed corundum samples is 31.07, 11.05 and 0.87 (average 14.33). This value for CBP samples is 11.03 and 10.93, for syenite from the main body at the contact with CBP dyke is 18.47, while it is 50.65-114.39 (average 69.76) for the tourmaline sample. Similarity in REE behavior in syenite, CBP and corundum and their different behavior in tourmaline testify for a different (late) origin for tourmaline-quartz symplectites.

Trace element contents in corundum is a factor of element accessibility during crystallization (Peucat et al., 2007). Substitution of the minor and trace elements create different colour in corundum. Some analyzed spots in the corundums have exceptionally high Nb (192-780

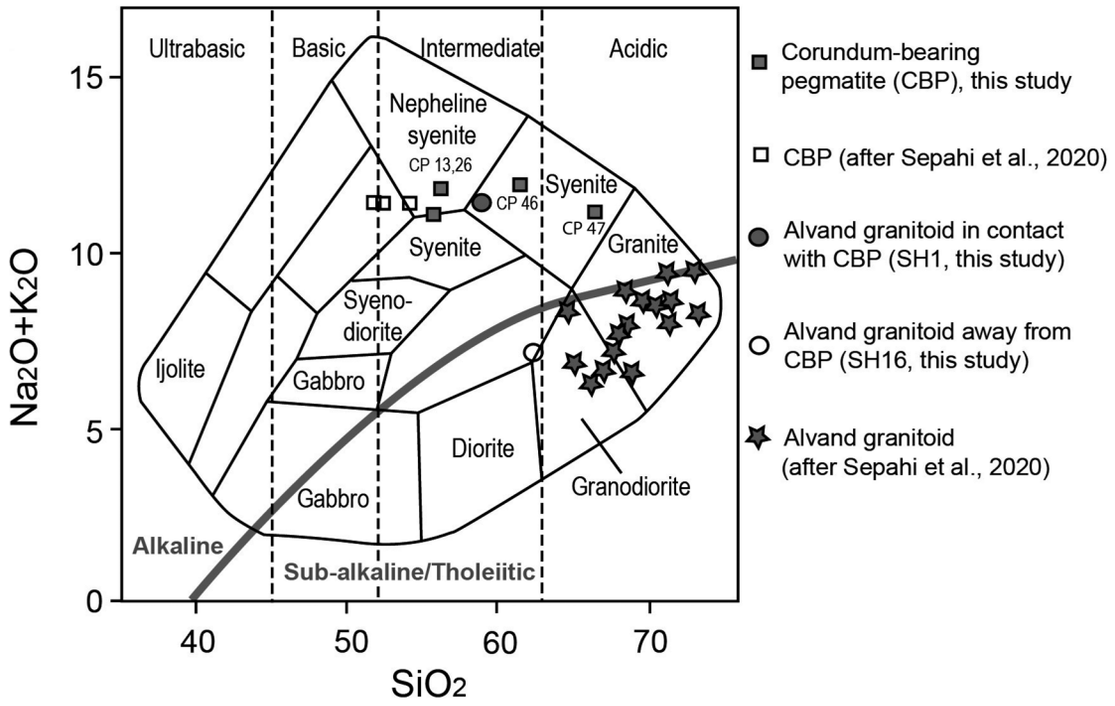


Figure 3. Plot of chemical compositions of Alvand granitoids and CBP on chemical classification diagram of Cox et al. (1979).

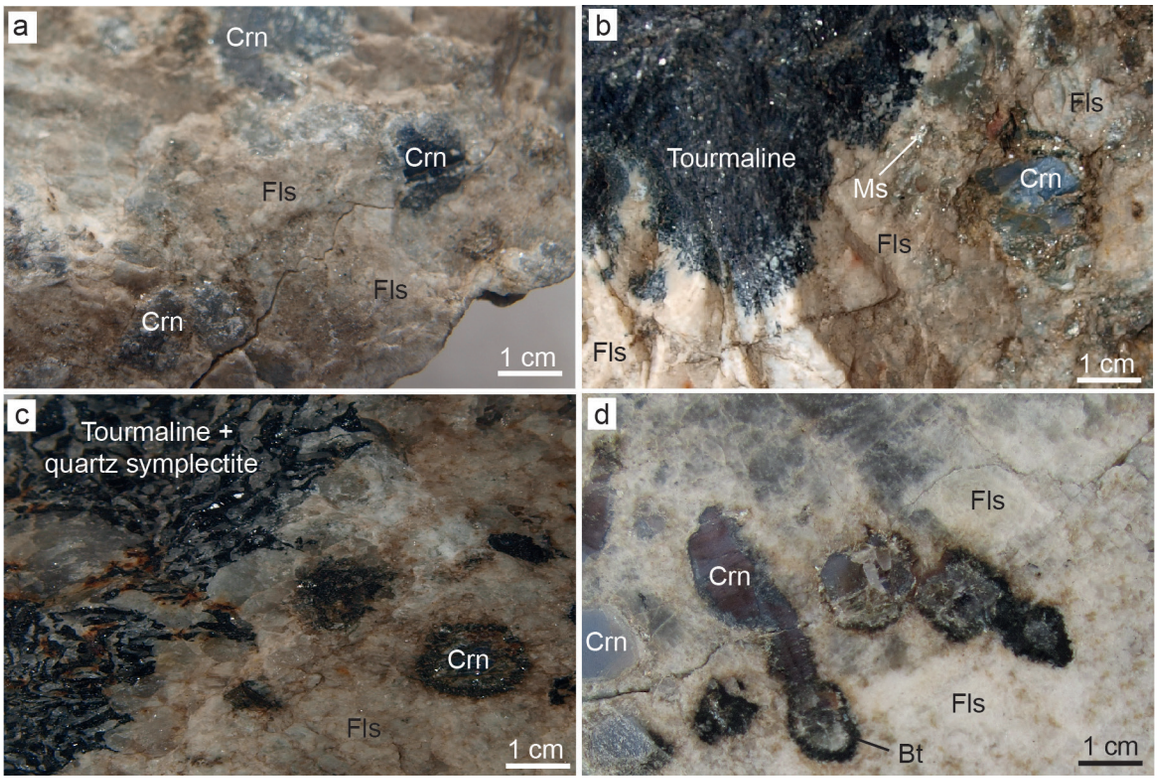


Figure 4. (a) A hand specimen of corundum-bearing syenite pegmatite with pale grey and dark corundum crystals (b) Tourmaline and muscovite in the sample along with corundum and feldspar (c) Tourmaline and quartz symplectite. There is no direct contact between quartz and corundum (d) A polished slab of a hand specimen showing pale grey and dark blue-grey corundum, surrounded by phlogopite. Mineral name abbreviations are from Whitney and Evans (2010).


Figure 5. (a) Corundum crystals, some separated from the rock samples. (b) A piece of translucent corundum with intergrowth of some crystals (two barrel-shaped crystals and some parts of one crystal with 120-degree growth lines. (c) A hand specimen of corundum-bearing rock with high amount of corundum. 120-degree growth lines is shown in one of the crystals. (d) Trapiche-like feature of a corundum crystal. (d) A pendent with cabochon polish made from translucent Hamedan corundum with blue colour and trapiche-like feature.

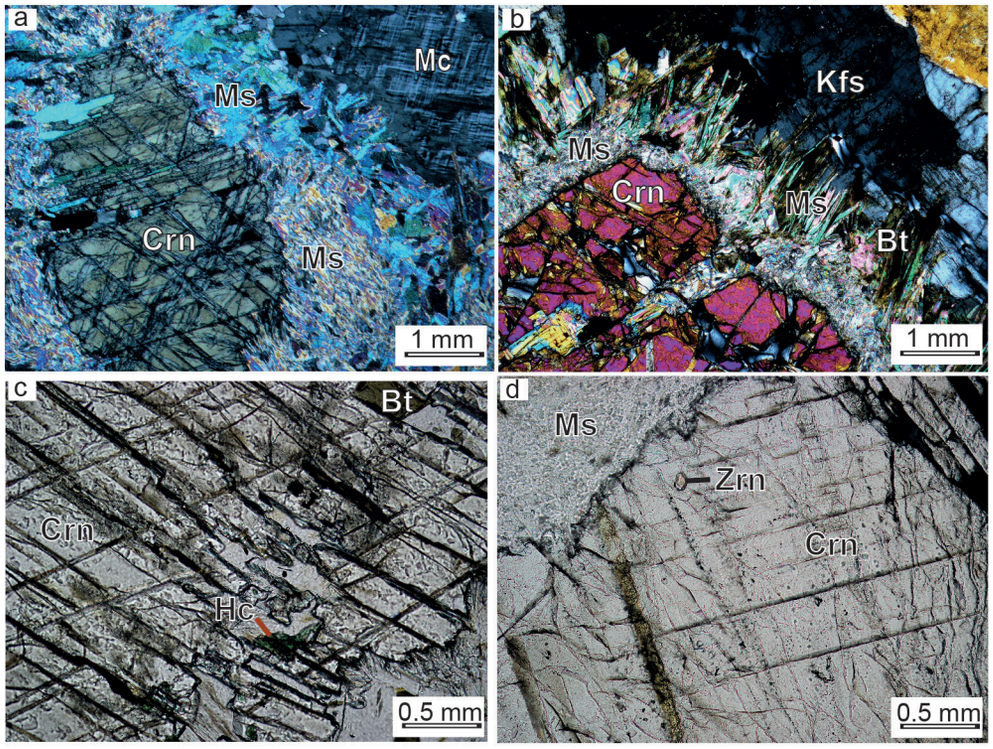


Figure 6. Minerals and textures of the corundum bearing samples under the microscope. (a) Corundum and K-feldspar in the sample with granular texture. Corundum is rimmed by secondary muscovite (cross polarized light). (b) Corundum surrounded by fine-grained muscovite (sericite) in the inner rim and coarser epitaxial muscovite at the outer rim (cross polarized light). (c) Hercynite inclusion and (d) zircon inclusion in corundum (both plain polarized light).

ppm) and Ta (311-1138 ppm) contents. Chemistry of host syenite pegmatite also shows high Nb and Ta contents (unpublished data by the authors). Some Nb and Ta oxides are formed as inclusions in the corundum crystals due to this enrichment. Colour in corundum is a function of different elements substitution in the mineral structure. Blue colour is a result of charge transfer process involving $Ti^{4+}$-$Fe^{2+}$ and $Fe^{2+}$-$Fe^{3+}$ pairs (Fritsch and Rossman,

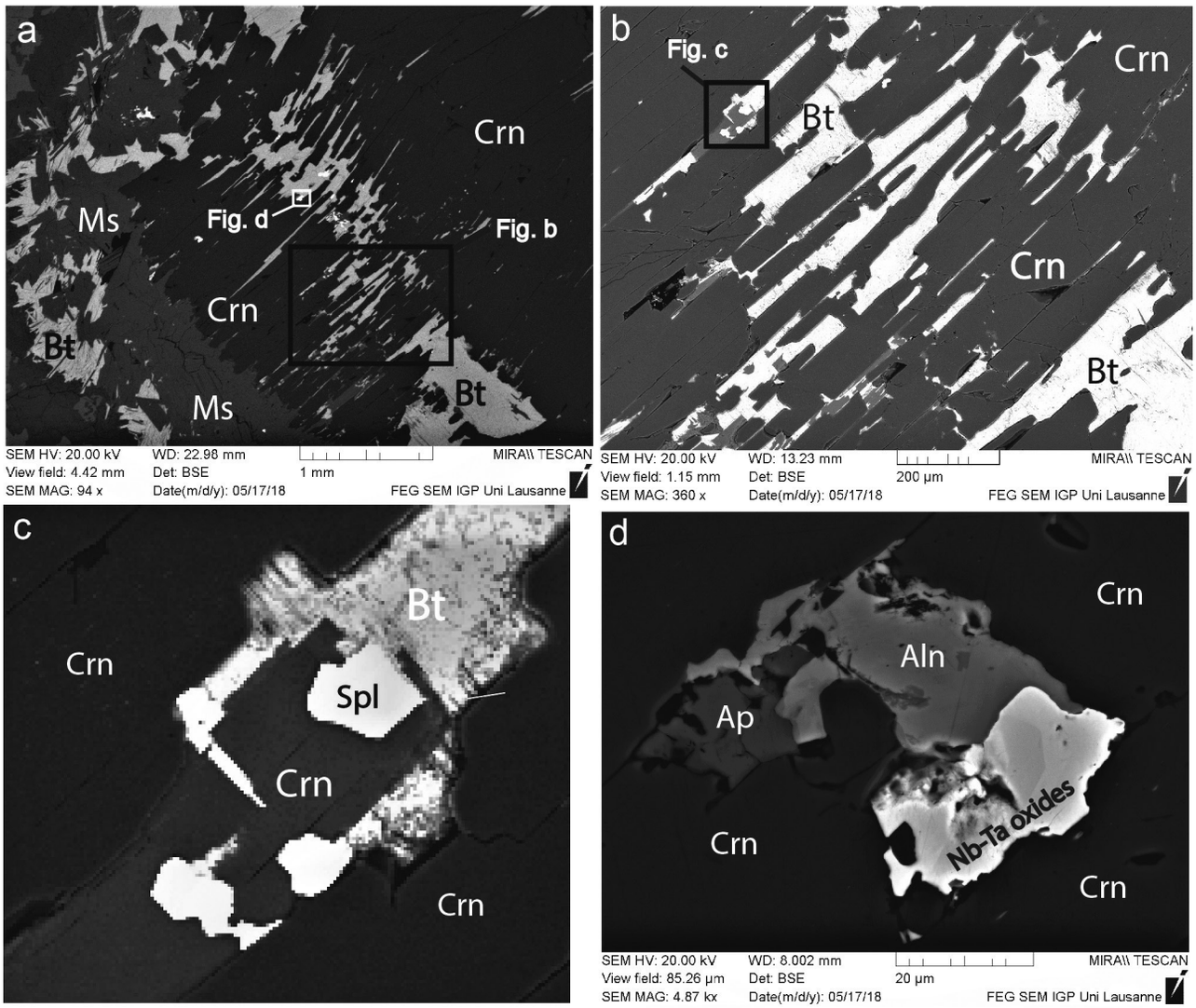


Figure 7. Secondary electron microscope (SEM) images from the studied corundum crystals. The main inclusions are biotite (a, b and c), spinel (c), Nb-Ta oxides, apatite and allanite (d).

1988). In order to study the element substitution causing blue colour in the Hamedan corundums, a crystal with colour zones was analyzed by EPMA along a profile across the colour zones (Figure 9a). The colour zones are indicated on the back scattered image. The diagram in Figure 9 b,c clearly shows correlation of the Ti and Ti/Fe content in corundum and the blue colour saturation. Grey to pale blue zones usually show low Fe concentrations, but this is not a general feature (Figure 9d). Ti content on creation of blue colour is more pronounced. Ti content across the zoning profile is variable from low to high. This can be explained by availability of Ti during corundum crystallization from the alkaline syenite magma.

Some indicative elements such as Mg, Ga, Ti and Fe can be used to decipher the magmatic versus metamorphic origin for corundum (Zaw et al., 2006; Peucat et al., 2007; Sutherland et al., 2008, 2009). Fe versus Ga/Mg binary and Fe-Mg-Ti ternary diagrams are used in this regard. Fe/Mg ratio is 168-861, Fe/Ti ratio is 0.6-23) and Ti/Mg ratio is 18-803. Ga/Mg ratio higher than 6 points to igneous origin for the studied corundums. Cr/Ga ratio lower than 1 is also an indicative of igneous corundums. The average of this ratio for our samples is 0.07, in accordance with igneous origin. Data from the studied samples are plotted in the Fe versus Ga/Mg diagram (Peucat et al., 2007; Southerland et al., 2008, 2009) in Figure 10a. Data from blue sapphires from alkali rocks of the SE Asia and China (the main Asian field, MAF, Peucat

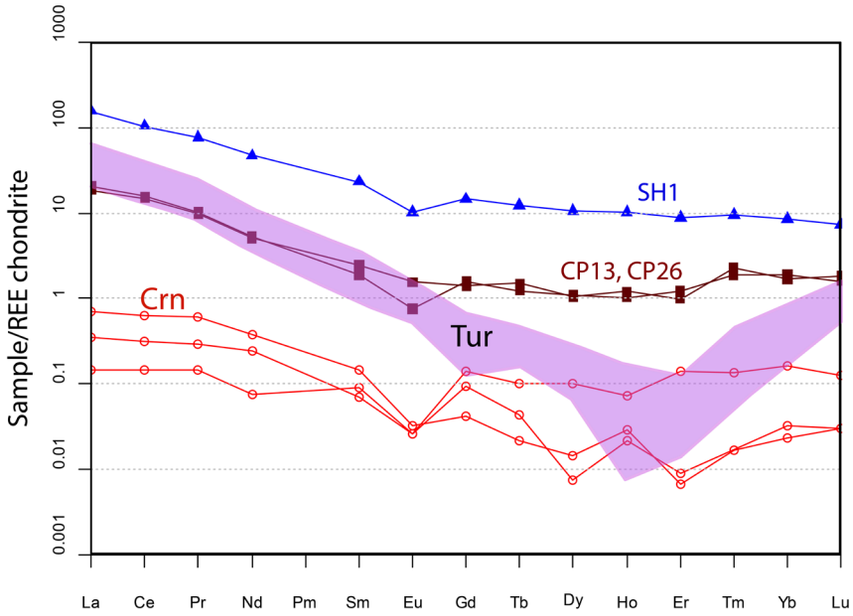


Figure 8. Chondrite-normalized REE diagrams for Alvand granitoid in contact with CBP (SH1), CBP (CP13,26), corundum (Crn) and tourmaline in CBP (Tur) (normalized to Nakamura, 1974 values).

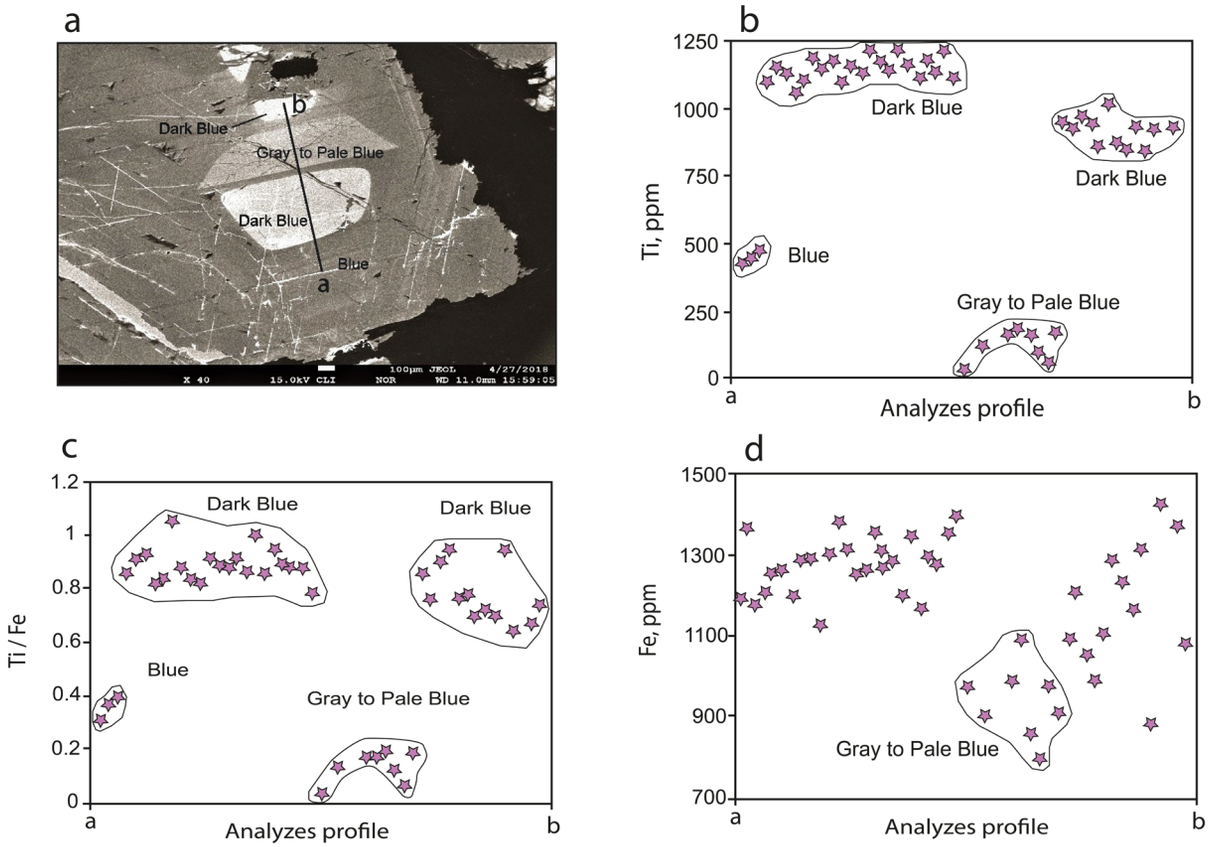


Figure 9. Analyzes of corundum with different coloured zones along a profile (a), Ti content (b), Ti/Fe ratio (c) and Fe content (d) based on EMPA results. Darker zones have higher Ti content and also Ti/Fe ratio.

et al., 2007) blue sapphires in Garba Tula monzonite in Kenya (Peucat et al., 2007), blue sapphires in Ilmen syenite pegmatite of Ural Mountains in Russia (Sorokina et al., 2017) and blue sapphires in the metamorphic rocks of the Ilmen area (Sorokina et al., 2019) are shown for comparison. The studied samples plot in the magmatic field in this figure. Compared to other blue sapphires shown in the diagram of Figure 10a, Hamedan corundums contain lower Fe and Mg, while have higher Ga contents. Notable they are distinctly different from Garba Tula sapphires in Fe, Mg and Ga contents. The studied samples plot in the igneous field of the Fe-Mg-Ti diagram of Peucat et al. (2007) in Figure 10b. Hamedan samples plot close to the Ti corner in this diagram, distinctly different from Garba Tula and Ilmen sapphires. In summary, the Hamedan blue corundums are formed from a syenite magma. $Ti^{4+}$-$Fe^{2+}$ exchange in these crystals is the main factor controlling the blue colour saturation.

ACKNOWLEDGEMENTS

This contribution is a part of the Ph.D. thesis of the first author in University of Tabriz. We are indebted to helps and supports from Prof. Lukas Baumgartner. We would like to thank Mr. Parchami and Mr. Torkaman from the Persian Yaghut Co. for introducing the filed area and Mr. Ahmadi for his helps during the field studies. Thanks are due to B. Putlitz, L. Nicod, M. Robyr, A. Ulianov, O. Reubi and P. Vonlanthen from the University of Lausanne for their help in preparing the samples and analyzes. We thank Prof. William Griffin for his review and valuable comments. The firs author would like to thank her husband Mr. Amir Emamjomeh for his helps during field and laboratory studies.

We thank editorial helps form Luca Bindi and Laura Teresa Di Pietro.

## REFERENCES

Armstrong J.T., 1995. CITZAF- a package of correction program for the quantitative electron microbeam X-ray analysis of thick polished materials, thin films and particles. Microbeam Analysis 4, 177-200.

Aydoğan M.S. and Moazzen M., 2012. Origin and Metamorphism of Corundum-Rich Metabauxites at Mt. Ismail in the Southern Menderes Massif, SW Turkey. Resource Geology 62, 243-262.

Baharifar A.A., Moinevaziri H., Bellon H., Pique A., 2004. The crystalline complexes of Hamadan (Sanandaj-Sirjan Zone, Western Iran): metasedimentary Mesozoic sequences affected by Late Cretaceous tectono-metamorphic and plutonic event. Comptes Rendus Geosciences 336, 1443-1452.

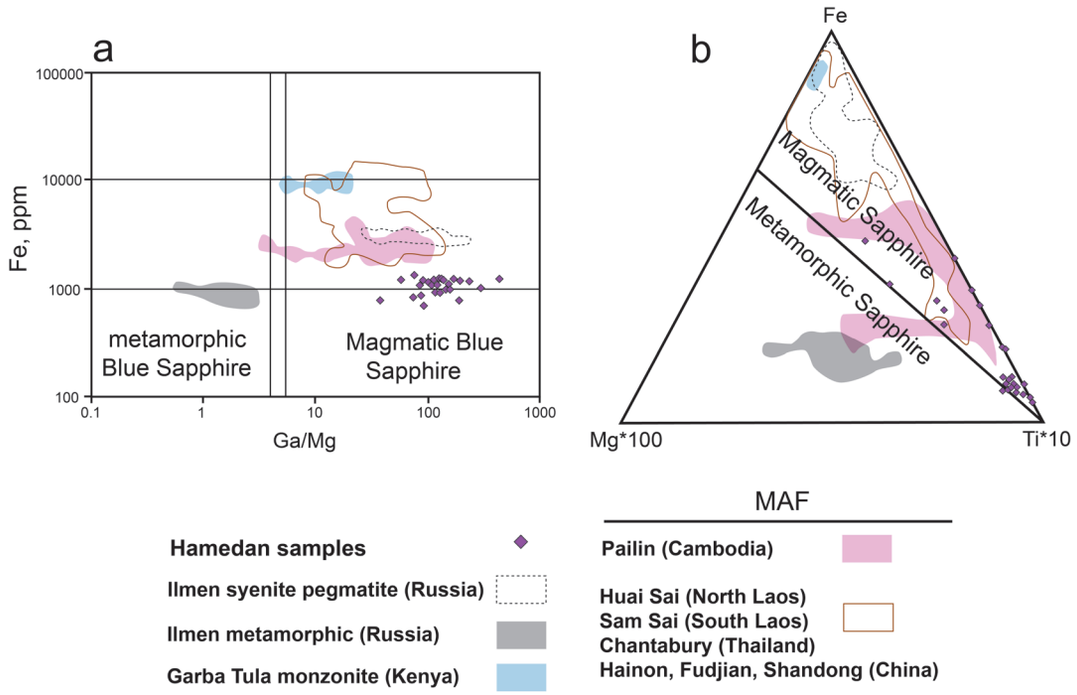


Figure 10. The studied corundum crystals show magmatic origin in Fe versus Ga/Mg diagram (a; after Peucat et al., 2007; Southerland et al., 2008; 2009) and Fe-Mg-Ti ternary diagram (b; after Peucat et al., 2007). Magmatic blue sapphires from SE Asia and China (MAF): (Pailin, Combodia; Houai Sai, N Laos; Sam Sai, S Laos; Chantaburi, Thailand and Hainan, Fudjian, Shandong, China) and sapphire in monzonite from Garba Tula, Kenya (all modified after Peucat et al., 2007), Ilmen syenite pegmatite, southern Urals, Russia, (modified after Sorokina et al., 2017) and metamorphic bleu sapphire from Ilmen metamorphic, southern Urals, Russia, (modified after Sorokina et al., 2019).

Bottrill R., 1998. A corundum-quartz assemblage in altered volcanic rocks, Bond Range, Tasmania. Mineralogical Magazine. 62, 325-332.

Cesbron F., Lebrun P., Le CLÉAC'H J.M., Notari F., Grobon C., Deville J., 2002. Corindons et spinelles. Minéraux et Fossiles 15, Paris, France.

Cox K.G., Bell J.D., Pankhurst R.J., 1979. The Interpretation of Igneous Rocks, London: Allen & Unwin.

Deer W.A., Howie R.A., Zussman J., 1992. An Introduction to the Rock-Forming Minerals. Longman Scientific and Technical, New York.

Droop G.T.R. and Moazzen M., 2007. Contact metamorphism and partial melting of Dalradian pelites and semipelites in the southern sector of the Etive aureole. Scottish Journal of Geology 43, 155-179.

Feenstra A., 1996. An EMP and TEM-AEM study of margarite, muscovite and paragonite in polymetamorphic metabauxites of Naxos (Cyclades, Greece) and the Implications of fine-scale mica interlayering and multiple mica generations. Journal of Petrology 37, 201-233.

Fritsch E. and Rossman G.R., 1988. An update on color in gems part 2, Colors involving multiple atoms and color centers. Gems and Gemology 24, 81-102.

Giuliani G. and Pignatelli I., 2016. "Trapiche" vs. "Trapiche-like" textures in minerals. InColor 31, 45-46.

Giuliani G., Ohnenstetter D., Fallick A.E., Groat L., Fagan A., 2014. Chapter: The geology and genesis of gem corundum deposits, In: Geology of Gem Deposits Series 2, 2nd Edition, Mineralogical Association of Canada.

Graham I., Sutherland F.L., Zaw K., Nechaev V., Khanchuk A., 2008. Advances in our understanding of the gem corundum deposits of the West Pacific continental margins intraplate basaltic fields. Ore Geology Reviews 34, 200-215.

Grice J.D., 1989. Bancroft: the Mineral Capital of Canada. In: Famous mineral localities of Canada. Fitzhenry & Whiteside Limited & the National Museum of Natural Sciences, 190 pp., 92-99; 162-165.

Guiraud M., Kienast J.R., Ouzegane K., 1996. Corundum-quartz-bearing assemblage in the Ihouhaouene area, in Ouzzal (Algeria). Journal of Metamorphic Geology 14, 755-761.

Guo J., O'Reilly S.Y., Griffin W.L., 1996. Corundum from basaltic terrains: a mineral inclusion approach to the enigma. Contributions to Mineralogy and Petrology 122, 368-386.

Kelly M.M. and Harley S.L., 2004. Orthopyroxene-Corundum in Mg-Al-rich Granulites from the Oygarden Islands, East Antarctica. Journal of Petrology 45, 1481-1512.

Kievlenko E.Y., 2003. Geology of Gems. Ocean Pictures Ltd, Littleton, CO, USA.

Klein C. and Hurlbut C.S.,1993. Manual of Mineralogy. John Wiley and Sons, New York.

Mehdipour Ghazi J. and Moazzen M., 2015. Geodynamic evolution of the Sanandaj-Sirjan Zone, Zagros Orogen, Iran. Turkish Journal of Earth Science 24, 513-528.

Mohajjel M., Fergusson C.L., Sahandi M.R., 2003. Cretaceous-Tertiary convergence and continental collision, Sanandaj-Sirjan Zone, Western Iran. Journal of Asian Earth Sciences 21, 397-412.

Mohajjel M. and Fergusson C.L., 2000. Dextral transpression in Late Cretaceous Continental Collision, Sanandaj-Sirjan Zone, Western Iran. Journal of Structural Geology 22, 1125-1139.

Motoyoshi Y., Hensen B.J., Matsueda H., 1990. Metastable growth of corundum adjacent to quartz in a spinel-bearing quartzite from the Archaean Napier Complex, Antarctica. Journal of Metamorphic Geology 8, 125-130.

Nakamura N., 1974. Determination of REE, Ba, Fe, Mg, Na and K in carbonaceous and ordinary chondrites. Geochimica et Cosmochimica Acta 38, 757-775.

Peucat J.J., Ruffaut P., Fritsch E., Bouhnik-Le E., Simonet C., Lasnier B., 2007. Ga/Mg ratio as new geochemical tool to differentiate magmatic from metamorphic blue sapphire. Lithos 98, 261-271.

Saki A., Moazzen M., Baharifar A.A., 2012. Migmatite microstructures and partial melting of Hamadan metapelitic rocks, Alvand contact aureole, western Iran. International Geology Review 54, 1229-1240.

Schmetzer K., 1987. On twinning in natural and synthetic flux-grown ruby. Journal of Gemology 20, 294-305.

Sepahi A A., Whitney D.L., Baharifar A.A., 2004. Petrogenesis of andalusite-kyanite-sillimanite veins and host rocks, Sanandaj-Sirjan metamorphic belt, Hamadan, Iran. Journal of Metamorphic Geology 22, 119-134.

Sepahi A.A., Jafari S.R., Osanai Y., Shahbazi H., Moazzen M., 2018. Age, petrologic significance and provenance analysis of the Hamedan low-pressure migmatites Sanandaj-Sirjan zone, west Iran. International Geology Review, https://doi.org/10.1080/00206814.2018.1517392.

Sepahi A.A., Vahidpour H., David R.L., McFarlane C.R.M., Maanijou M., Salami S., Miri M., Mansouri M., Mohammadi R., 2020. Rare sapphire-bearing syenitoid pegmatites and associated granitoids of the Hamedan region, Sanandaj-Sirjan zone, Iran: analysis of petrology, lithogeochemistry and zircon geochronology/trace element geochemistry. Geological magazine, https://doi.org/10.1017/S0016756820000023.

Shahabpour J., 2005. Tectonic evolution of the orogenic belt in the region located between Kerman and Neyriz. Journal of Asian Earth Sciences 24, 405-417.

Shahbazi H., Siebel W., Pourmoafee M., Ghorbani M., Sepahi A.A., Shang C.K., Vousoughi Abedini M., 2010. Geochemistry and U-Pb zircon geochronology of the Alvand plutonic complex in Sanandaj-Sirjan Zone (Iran): New evidence for Jurassic magmatism. Journal of Asian Earth Sciences 39, 668-683.

Simonet C., Fritsch E., Lasnier B., 2008. A classification of gem corundum deposits aimed towards gem exploration. Ore Geology Reviews 34, 127-133.

Simonet C., Paquette J.L., Pin C., Lasnier B., Fritsch E., 2004.

The Dusi (Garba Tula) sapphire deposit, Central Kenya-a unique Pan-African corundum-bearing monzonite. Journal of African Earth Sciences 38, 401-410.

Sorokina E.S., Karampelas S., Nishanbaev P., Nikandrov S.N., Semiannikov B.S., 2017. Sapphire megacrysts in syenite pegmatites from the Ilmen mountains, south Urals, Russia: New mineralogical data. The Canadian Mineralogist 55, 823-843.

Sorokina E.S., Rassomakhin M.A., Nikandrov S.N., Karampelas S., Kononkova N.N., Nikolaev A.G., Anosova M.O., Somsikova A.V., Kostitsyn Y.A., Kotlyarov V.A., 2019. Origin of Blue Sapphire in Newly Discovered Spinel-Chlorite-Muscovite Rocks within Meta-Ultramafites of Ilmen Mountains, South Urals of Russia: Evidence from Mineralogy, Geochemistry, Rb-Sr and Sm-Nd Isotopic Data. Minerals 9(36), 1-23.

Sutherland F.L., Duroc-Danner J.M., Meffre S., 2008. Age and origin of gem corundum and zircon megacrysts from the Mercaderes-Rio Mayo area, South-west Colombia, South America. Ore Geology Review 34, 155-168.

Sutherland F.L., Zaw K., Meffre S., Giuliani G., Fallick E.A., Graham T.I., Webb B.G., 2009. Gem corundum megacrysts from east Australia basaltic fields: trace elements, oxygen isotopes and origin. Australian Journal of Earth Sciences 56, 1003-1022.

Sutherland F.L., Hoskin P.W.O., Fanning C.M., Coenraads R.R., 1998. Models of corundum origin in alkali basaltic terrains, a reappraisal. Contributions to Mineralogy and Petrology 133, 356-372.

Sutthirat C., Saminpanya S., Droop G.T.R., Henderson C.M.B., Manning D.A.C., 2001. Clinopyroxene-corundum assemblages from alkali basalt and alluvium, eastern Thailand: constraints on the origin of Thai rubies. Mineralogical Magazine 65, 277-295.

Vysotskiy S.V., Nechaev V.P., Kissin A.YU., Yakovlenko V.V., Velivetskaya T.A., Sutherland F.L., Agoshkov A.I., 2015. Oxygen isotopic composition as an indicator of ruby and sapphire origin: A review of Russian occurrences. Ore Geology Reviews 68, 164-170.

Whitney D.L. and Evans B.W., 2010. Abbreviations for names of rock-forming minerals. American Mineralogist 95, 185-187.

Zaw K., Sutherland F.L., Dellapasqua F., Ryan G.C., Tzen-Fu Y., Mernagh P.T., Duncan D., 2006. Contrasts in gem corundum characteristics, eastern Australian basaltic fields: trace elements, fluid/melt inclusions and oxygen isotopes. Mineralogical Magazine 70, 66.